

Article

Coupled CFD-DEM Simulation of Seed Flow in Horizontal-Vertical Tube Transition

Leno Guzman, Ying Chen ^{*ID} and Hubert Landry

Department of Biosystems Engineering, University of Manitoba, Winnipeg, MB R3T 5V6, Canada

* Correspondence: ying.chen@umanitoba.ca

Abstract: A series of computational fluid dynamics–discrete element method (CFD-DEM) simulations were applied to seed flow in horizontal-vertical 90-degree elbows. The performance of one-way and two-way CFD-DEM coupling methods was compared. Additionally, simulated seed velocities were compared to the current pneumatic conveying theory for each coupling method. Simulated field peas (*Pisum sativum*) were pneumatically conveyed to study the effect of air velocity (20, 25, and 30 m/s), seed rate (0.07, 0.21, and 0.42 kg/s), elbow diameter, D , (48.3, 60.3, and 72.4 mm), and elbow bend radius (1.5 D , 2.5 D , 3.5 D , and 4.5 D) on seed attributes (trajectory, velocity, and force). Results showed that seed velocity was significantly different between one-way and two-way coupling. Both methods resulted in nearly identical seed trajectory and force. Overall, simulated seed velocities had a strong correlation to values calculated through the current pneumatic conveyance theory. Dimensional analysis revealed that seed contact force was proportional to the elbow diameter to the power of 0.26 and inversely proportional to the elbow bend radius to the power of 0.5. Simulation results indicated that one-way coupling could be suitable to describe seed flow when two-way coupling may not be possible or practical.

Keywords: seed; pneumatic conveyance; discrete element method; computational fluid dynamics; simulation



Citation: Guzman, L.; Chen, Y.; Landry, H. Coupled CFD-DEM Simulation of Seed Flow in Horizontal-Vertical Tube Transition. *Processes* **2023**, *11*, 909. <https://doi.org/10.3390/pr11030909>

Academic Editor: Alberto Di Renzo

Received: 16 February 2023

Revised: 8 March 2023

Accepted: 10 March 2023

Published: 16 March 2023



Copyright: © 2023 by the authors. Licensee MDPI, Basel, Switzerland. This article is an open access article distributed under the terms and conditions of the Creative Commons Attribution (CC BY) license (<https://creativecommons.org/licenses/by/4.0/>).

1. Introduction

Pneumatic conveyance is an integral part of seed handling in agriculture. In the context of air seeding, seeds are subjected to various pneumatic conveyance situations including horizontal flow, horizontal-vertical elbow transitions, and distribution into multiple outlets. Seed flow conditions at horizontal-vertical elbow transitions result in a significant seed velocity reduction due to collisions with the outer elbow wall [1]. This type of collision with machine surfaces may result in mechanical damage [2] and influence important seed attributes, such as seed germination and vigor index [3]. A better understanding of gas–solid flow characteristics in pneumatic conveyance has the potential to influence the approach to designing processes and equipment.

Fluid mechanics fundamentals can generally describe gas–solid flows, but theoretical predictions are often not applicable to transition regions of interest. Experimental studies including the use of laser light sheet flow visualization methods [4], high-speed cameras [5], and pressure sensors [6] provide valuable data to expand our knowledge of gas–solid flow behaviors. However, experimental techniques are not easily applicable to many complex gas–solid flow conditions. Computer simulation methods [7] are useful in representing gas–solid flows where general pneumatic conveyance theory and experimentation are not practical. A combination of computational approaches and novel experimentation is required to keep this research field progressing [8,9].

Computer simulations are well suited to the study of pneumatically conveyed seeds due to their ability to capture detailed seed attributes, such as trajectory, velocity, and force. Continuum models based on computational fluid dynamics (CFD) and the application of

Eulerian–Lagrangian methods [10,11] are among the most common approaches to model the types of gas–solid flows present in pneumatic conveying systems [7]. Of particular interest to this study is the application of CFD coupled with the discrete element method (DEM) because individual particle collisions are simulated through well-established contact models [10,12,13]. Hence, this method allowed for the detailed examination of seed collision events in areas of interest such as horizontal-vertical elbow transitions. This approach is advantageous for the selection of elbow design features and operational conditions that could minimize seed damage.

There is a high computational cost associated with the application of CFD-DEM relative to other Lagrangian approaches that do not consider individual particle collisions or the effect of particles on the fluid phase. The use of CFD-DEM coupling that considers the effect of particles in the fluid phase and vice versa is known as two-way coupling. A common implementation of two-way CFD-DEM coupling known as the coarse-grid approach incorporates fluid cells that are several times larger than the particle size [14,15]. This implementation attempts to balance fluid flow resolution and computation speed. However, the grid size requirements can sometimes result in inaccuracies in predicting the fluid phase [16]. An example of this limitation applies to air seeding distribution systems, more specifically vertical seed distributor heads.

Air seeder distributor heads normally consist of tubing with a horizontal-vertical 90-degree elbow transition that divides the flow of seed into multiple outlets at the end of the vertical tube section. The ratio of commonly used tubing size to agricultural seed diameters is not ideal for the requirements of the coarse-grid approach. Considering solid loading ratios in air seeders are commonly within the dilute phase, there is an opportunity to use one-way coupled CFD-DEM simulations. One-way CFD-DEM coupling includes the effect of fluid force (air) on particles (seeds), but the effect of particles on the fluid is assumed negligible. One-way coupled CFD-DEM is not affected by the ratio of CFD element size to particle size and has been shown to perform well in simulations with small particles, such as sand [17]. However, there is limited data comparing one-way and two-way coupling for particles in the agricultural seed size range. Furthermore, research studies that examine particle impacts in horizontal-vertical elbow flow often focus on erosion [18,19] rather than monitoring individual particle forces.

The main goal of this study was to evaluate one-way CFD-DEM coupling applied to seed pneumatic conveyance on a horizontal-vertical 90-degree elbow. More specifically, the objectives were to (1) examine the effect of various pneumatic conveying conditions (seed rate, air velocity, and elbow bend radius and diameter) on seed attributes (i.e., trajectory, velocity, and forces), (2) compare simulated seed velocities to currently available pneumatic conveying theory, and (3) compare simulated seed attributes from one-way CFD-DEM coupling with two-way coupling.

2. Materials and Methods

2.1. Simulation Geometry and Seed

Air seeders have several features that work together to deliver a prescribed amount of seed into agricultural fields. The pneumatic conveyance systems found in air seeder designs vary by manufacturer but typically include a central seed storage tank with a seed metering mechanism, a series of horizontal distributor tubes that pneumatically convey seed from the storage tank to a seeding implement, and a seed manifold attached to the end of each distributor tube which further separates seeds into distinct rows for incorporation into the soil. The transition between the horizontal seed distributor tube and the seed manifold in the implement is commonly achieved through horizontal–vertical elbows (Figure 1a). Typical elbow transitions in air seeders have short vertical sections (approximately 0.5 m) and include geometric features (e.g., dimples or corrugations) to enhance seed distribution uniformity within the tube cross-section. For this study, simulated green field pea (*Pisum sativum*) seeds were introduced into a horizontal-vertical 90-degree elbow

(Figure 1b). The vertical tube section had an extended length and smooth walls to allow seed velocity comparisons between simulations and pneumatic conveyance theory.

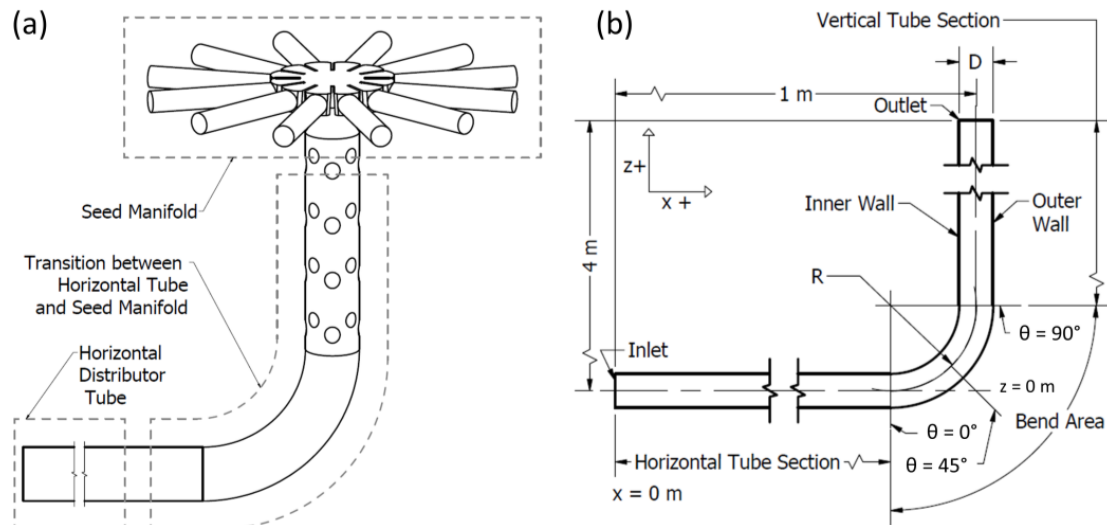


Figure 1. Horizontal-vertical 90-degree elbow transition: (a) typical air seeder system, and (b) simulation geometry.

2.2. Model Development

Physical material properties, initial boundary conditions, and input parameters define the overall simulation behavior. Model development included simulation parameters for two phases, solid and fluid. The solid phase (seed and elbow boundaries) was simulated with DEM software, Particle Flow Code in Three Dimensions (PFC3D) (Itasca Group, Minneapolis, MN, USA). Elbow boundaries were generated as a DEM wall and seeds were represented as DEM balls. The fluid phase (air) was simulated with CFD software, OpenFOAM (ESI Group, Paris, France). The main details of operating each software, including simulation parameters as well as the coupling method, are described in the following sections. Additional information related to the numerical methods for each solver is available as part of the Supplementary Material.

2.2.1. DEM Contact Model Parameters

The Hertz contact model was selected to simulate seed–seed and seed–wall collisions. Seed contact properties were assigned a set of experimental and calculated values from the literature (Table 1). Tube walls were assigned material properties of mild steel. Contact model properties for particles (seeds) and walls (steel tube) were explicitly assigned. The particle–wall friction coefficient, μ_{p-w} , and coefficient of restitution were assigned from the literature [20,21]. The energy dissipation between contacts was achieved through the application of the hysteresis damping formulation in PFC3D. Contact property modeling for particle–particle and particle–wall interactions were derived implicitly through surface property inheritance. Shear modulus and Poisson’s ratio were calculated by the average of the contacting piece values, as follows [22]:

$$v_{contact} = \frac{4G^* - E^*}{2G^* - E^*} \quad (1)$$

$$G_{contact} = 2G^*(2 - v_{contact}) \quad (2)$$

$$E^* = \left(\frac{1 - \nu^{(1)}}{2G^{(1)}} + \frac{1 - \nu^{(2)}}{2G^{(2)}} \right)^{-1} \quad (3)$$

$$G^* = \left(\frac{2 - \nu^{(1)}}{G^{(1)}} + \frac{2 - \nu^{(2)}}{G^{(2)}} \right)^{-1} \quad (4)$$

where $\nu_{contact}$ is the Poisson's ratio at the interaction between two bodies, $G_{contact}$ is the shear modulus (Pa) at the interaction between two bodies, G^* is the effective shear modulus (Pa), E^* is the effective modulus of elasticity (Pa), and the superscripts (1) and (2) denote contacting bodies 1 and 2, respectively.

Table 1. Discrete element method (DEM) input parameters.

Parameter	Symbol	Unit	Value	Reference
Particle Density, Pea Seed	ρ_p	kg/m ³	1720	[21]
Particle Diameter, Pea seed	d	mm	6.94	[23]
Modulus of Elasticity, Pea Seed	E_p	Pa	236×10^6	[20]
Shear Modulus, Pea Seed	P_g	Pa	98.3×10^6	Calculated from E_p
Modulus of Elasticity, Wall	E_w	Pa	200×10^9	-
Shear Modulus, Wall	G_w	Pa	76.8×10^9	Calculated from E_w
Poisson's Ratio, Pea Seed	ν_p	-	0.20	[20]
Poisson's Ratio, Wall	ν_w	-	0.30	-
Friction Coefficient (particle–wall)	μ_{p-w}	-	0.22	[21]
Friction Coefficient (particle–particle)	μ_{p-p}	-	0.24	[21]
Coefficient of Restitution	c	-	0.56	[20]

2.2.2. CFD Solver and Boundary Conditions

Airflow velocity and pressure fields were determined through the Navier–Stokes equations using the Reynolds-averaged Navier–Stokes (RANS) method with the realizable k- ϵ turbulence model. The realizable k- ϵ turbulence model was selected because it provided the most stable results for the whole range of simulated conditions.

The coarse-grid method used during two-way coupled simulations required CFD elements to be larger than the simulated seeds. Preliminary simulations were performed to determine the smallest mesh resolution that would provide stable results for the simulated seed size. Additional information regarding mesh sizing and discretization error approximation using the grid convergence index [24,25] is available as part of the Supplementary Material. The CFD mesh for each elbow geometry was composed of tetrahedral elements with a target length of approximately 10×10^{-3} m and a maximum element length of 15×10^{-3} m. The mesh for simulation sets 1 and 2 consisted of 79,670 elements (Figure 2). The meshes used in simulation set 3 differed for each geometry combination (i.e., bend radius and elbow diameter) and the number of elements ranged between 76,000 and 116,000.

The boundary regions were defined as (i) the inlet, where air and seeds are first introduced; (ii) the outlet, where the seeds and air exit the system; and (iii) the walls representing the solid boundaries of the simulated geometries. Figure 1b shows the relative locations of the boundary regions. The boundary regions were assigned values or boundary conditions (Table 2). The near-wall behavior of the turbulence model was approximated through wall functions. Details of the wall function formulation implemented in OpenFOAM are described by Kalitzin et al. [26]. Air density and kinematic viscosity were assigned values of 1.225 kg/m^3 and $1.470 \times 10^{-5} \text{ m}^2/\text{s}$, respectively. The values of k and ϵ at the inlet were calculated using the following relationships [27]:

$$k = \frac{3}{2} (U_{ref} T_i)^2 \quad (5)$$

$$\varepsilon = C_{\mu}^{3/4} \frac{k^{3/2}}{l} \quad (6)$$

$$l = 0.07L \quad (7)$$

where k is turbulent kinetic energy (m^2/s^2), U_{ref} is air velocity (m/s), T_i is turbulence intensity (0.05), C_{μ} is a constant (0.09), ε is the rate of dissipation of the turbulent kinetic energy (m^2/s^3), l is length scale (m), and L is characteristic length (m).

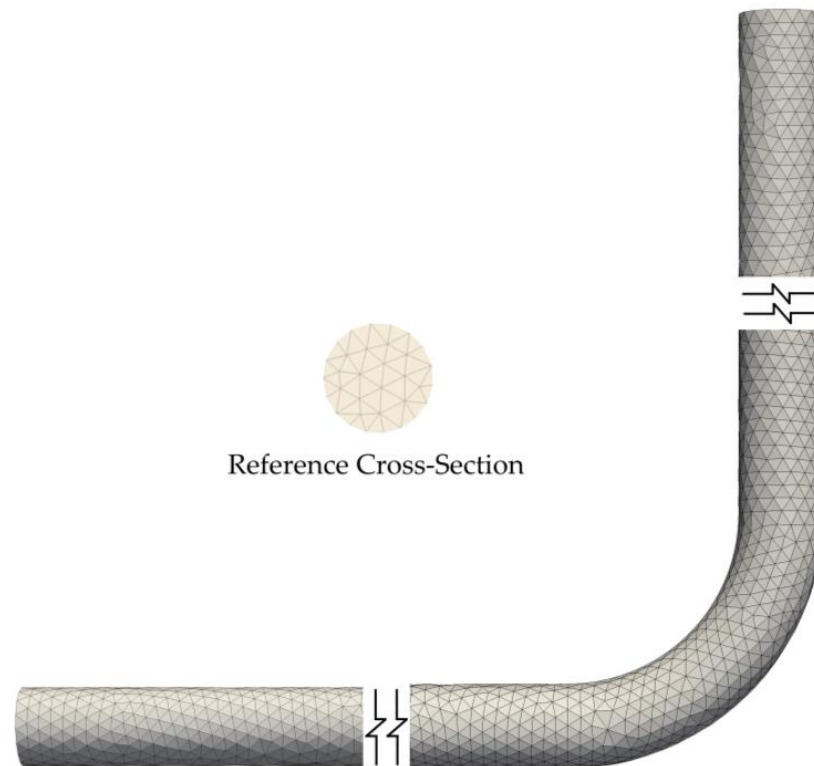


Figure 2. Sample computational fluid dynamics (CFD) mesh views: horizontal-vertical 90-degree elbow for simulation sets 1 and 2.

Table 2. Computational fluid dynamic (CFD) solver boundary conditions for air velocity (V_a), pressure (P), turbulent kinetic energy (k), and rate of dissipation of the turbulent kinetic energy (ε).

Region	V_a (m/s)	P (Pa)	k (m^2/s^2)	ε (m^2/s^3)
Inlet	20	Zero Gradient	1.50	71.87
	25		2.34	140.38
	30		3.38	242.57
Outlet	Zero Gradient	0	Zero Gradient	Zero Gradient
Wall	0	Zero Gradient	kWall Function	eWall Function

2.2.3. CFD-DEM Coupling

The CFD solver was linked with the DEM solver through one-way and two-way coupling methods. One-way coupling models the effect of fluid force (air) acting on particles (seeds), but the presence of seeds does not affect airflow movement, including the velocity and pressure fields of the air. Comparatively, two-way coupling modelled both air–seed and seed–air interactions. The p2pLink classes in the Python module of the DEM solver (PFC3D) were employed to exchange data between each software (OpenFOAM and PFC3D) in the Python environment. The reference diagram shown in Figure 3 serves as a tool to visualize the process, while the details of each coupling method are further explained in the following paragraphs.

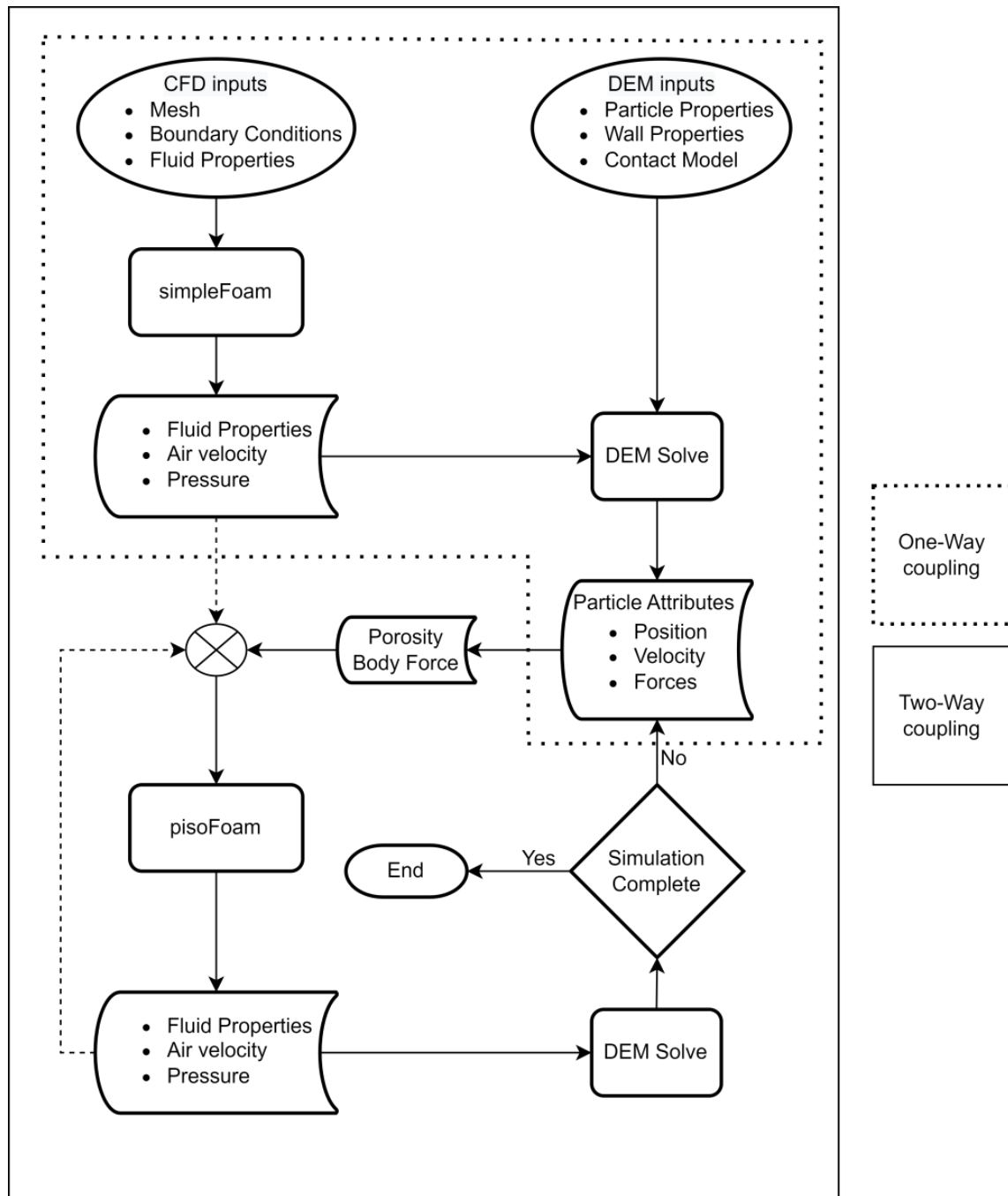


Figure 3. Reference diagram for one-way and two-way CFD-DEM coupling process.

The simpleFoam solver [28] was used to determine the steady-state airflow conditions. The simpleFoam solver is a steady-state solver for incompressible, turbulent flow that uses the Semi-Implicit Method for Pressure Linked Equations (SIMPLE) algorithm. The convergence criteria for the steady-state simulation were residuals of 10^{-3} for pressure and 10^{-4} for all other fluid fields. In one-way coupling, the steady-state airflow behaviour was imported into the DEM solver to simulate the fluid force effect on particles. The following equations summarize the relationships that govern the fluid force acting on particles within the DEM solver [22]:

$$\vec{f}_{fluid} = \left(\frac{1}{2} C_d \rho_f \pi r^2 |\vec{u} - \vec{v}| (\vec{u} - \vec{v}) \right) a^{-\lambda} + \frac{4}{3} \pi r^3 (\nabla p - \rho_f \vec{g}) \quad (8)$$

$$C_d = \left(0.63 + \frac{4.8}{\sqrt{Re_p}}\right)^2 \quad (9)$$

$$Re_p = \frac{2\rho_f r \left| \vec{u} - \vec{v} \right|}{\mu} \quad (10)$$

$$\chi = 3.7 - 0.65e^{\frac{(-1.5 \log_{10} Re_p)^2}{2}} \quad (11)$$

where \vec{f}_{fluid} is the fluid force acting on a particle (N), C_d is the dimensionless drag coefficient, ρ_f is the fluid density (kg/m^3), \vec{u} is the particle velocity (m/s), \vec{v} is the fluid velocity (m/s), α is the porosity, χ is the voidage function exponent, p is the fluid pressure (Pa), \vec{g} is the acceleration due to gravity (m/s^2), Re_p is the particle Reynolds number, and μ is the fluid dynamic viscosity ($\text{kg}/\text{m}\cdot\text{s}$).

One-way coupled simulations had a CFD timestep of 1×10^{-4} s. The DEM timestep ranged between 1×10^{-5} and 1×10^{-6} s. Determination of the DEM timestep size was automated through algorithms built into the PFC3D software. The timestep determination maintained 80% of the critical time step while considering all particle attributes. Each simulation consisted of 3 s of physical time. Particles (seeds) were introduced into the system for 1 s and allowed to flow through the geometry until exiting the system. The 3-s simulation time allowed all generated particles to exit the system by the end of each simulation.

In two-way coupled simulations, the steady-state airflow conditions extracted from the simpleFoam solver were used as the initial fluid field state. The airflow calculations for two-way coupling were solved as a transient-state simulation using a modified pisoFOAM solver. This transient solver for incompressible turbulent flow uses the Pressure-Implicit with Splitting of Operator (PISO) algorithm. The pisoFOAM solver included all the modifications originally made available by Itasca [29] with the addition of turbulence modelling for the airflow calculations.

Two-way coupling between CFD and DEM solvers was achieved through the application of the relationships described in Equations (8) to (11) and a modification of the Navier–Stokes equations for incompressible viscous flow. The modification incorporates the effect of a particulate solid phase mixed into the fluid and is described by the following equations:

$$\rho_f \frac{\partial \alpha \vec{v}}{\partial t} + \rho_f \vec{v} \cdot \nabla (\alpha \vec{v}) = -\alpha \nabla p + \mu \nabla^2 (\alpha \vec{v}) + \nabla \tau + \vec{f}_b \quad (12)$$

$$\frac{\partial \alpha}{\partial t} + \nabla \cdot (\alpha \vec{v}) = 0 \quad (13)$$

where α is the porosity, t is time (s), μ is the fluid dynamic viscosity ($\text{kg}/\text{m}\cdot\text{s}$), $\nabla \tau$ is the Reynolds stress term (N/m^3), and \vec{f}_b is the volume of the averaged body force (N/m^3).

Two-way coupled simulations had a CFD timestep of 1×10^{-4} s and a DEM timestep of 1×10^{-6} s. The coupling interval was the same as the CFD timestep, which resulted in 100 DEM timesteps for each CFD timestep. The DEM particle positions are used to determine porosity at each CFD element between coupling intervals. The porosity and body forces are transferred to the CFD solver (modified pisoFOAM) during each coupling interval to calculate the airflow characteristics for current particle positions. The airflow fields, pressure gradient and fluid velocity were then sent back to the DEM solver to be included in the force balance calculations that determine particle motion.

2.3. Simulation Description

Seeds were generated at the elbow inlet, 0.8 to 1 m away from the vertical tube centerline, at random positions within the lower half of the tube cross-section. The initial seed positions were determined based on previous simulation work describing horizontal

seed flow [30]. Initial seed velocities (Table 3) at the seed inlet approximated the expected steady-state horizontal seed velocity, which was calculated based on equations from Santo et al. [31,32].

Table 3. Simulation parameters for each simulation set.

Set	Parameter	Symbol	Unit	Value
1	Elbow Diameter	D	mm	60.3
	Elbow Bend Radius	R	mm	2.5D
	Air Velocity (Initial Seed Velocity)	$V_a (U_{p,i})$	m/s	20 (8.7)/25 (10.9)/30 (13.1)
	Seed Rate	\dot{m}_s	Kg/s	0.07
	Coupling Method	-	-	One-way/Two-way
2	Elbow Diameter	D	mm	60.3
	Elbow Bend Radius	R	mm	2.5D
	Air Velocity (Initial Seed Velocity)	$V_a (U_{p,i})$	m/s	25 (10.9)
	Seed Rate	\dot{m}_s	Kg/s	0.07/0.21/0.42
	Coupling Method	-	-	One-way
3	Elbow Diameter	D	mm	48.3/60.3/72.4
	Elbow Bend Radius	R	mm	1.5D/2.5D/3.5D/4.5D
	Air Velocity (Initial Seed Velocity)	$V_a (U_{p,i})$	m/s	25 (10.9)
	Seed Rate	\dot{m}_s	Kg/s	0.07
	Coupling Method	-	-	One-way

The flow behavior of seeds within the elbow was observed under different CFD-DEM simulation conditions, and the three sets of simulations were as follows: (1) tested the effect of air velocity and coupling method on seed position, velocity, and drag force; (2) examined the effect of seed rates on seed position and velocity; and (3) twelve elbow geometries, consisting of three bend radius and four elbow diameter combinations, were used in simulations with seeds flowing at the same air velocity and initial seed velocity to determine their effect on seed contact force at the bend area. The assigned values for air velocity, initial seed velocity, CFD-DEM coupling method, seed rate, elbow diameter, and elbow bend radius of each simulation set are summarized in Table 3. Average computation times in set 1 were 15 and 46 h for one-way and two-way coupled simulations, respectively (3.6 GHz Intel Core i7-7700 CPU).

2.4. Data Analysis

Simulated seed velocity results at the vertical tube section were compared to the average seed velocity calculated using a mathematical model developed by Tripathi et al. [5]; the mathematical model approximates the average seed velocity through the following equations:

$$BR_{H-V} = \frac{u_{B_0-V}}{u_{B_i-H}} \quad (14)$$

$$BR_{H-V} = 1.5Ar^{-[0.16 - (0.015)(\frac{R}{D}) + (6.3 \times 10^{-4})(\frac{R}{D})^2]} \left\{ 1 - e^{-[3 \times 10^{-5} Re_{p-ss-V}(\frac{D}{d})]} \right\} \quad (15)$$

$$Re_{p-ss-V} = \frac{\rho_p(v - u_t)d}{\mu} \quad (16)$$

$$u_t = 1.74 \sqrt{\frac{gd(\rho_p - \rho_f)}{\rho_f}} \quad (17)$$

$$\frac{L_{a-H}}{D} = 35 \cdot Ar^{0.113} \cdot \left(\frac{D}{D_{50}}\right)^{-1.45} \cdot (0.84 + 2.9 \times 10^{-6} \cdot Re_g) \quad (18)$$

$$\frac{u_{p-ss-H}}{v} = 1 - 0.02 \left[Ar \cdot \left(\frac{\rho_p - \rho_f}{\rho_f} \right) \cdot \left(\frac{D}{D_{50}} \right)^{-2} \right]^{0.14} \quad (19)$$

$$\frac{u_{p-H}}{u_{p-ss-H}} = \left(1 - e^{-\frac{x/L_{a-H}}{0.2}} \right) - 1.12 \cdot \left(\frac{x}{L_{a-H}} \right)^3 \cdot e^{-\frac{x/L_{a-H}}{0.2}} \quad (20)$$

$$\frac{u_{p-V}}{u_{p-ss-V}} = \left(1 - e^{-\frac{z/L_{a-V}}{0.11}} \right) - 30 \left(\frac{z}{L_{a-V}} \right)^{2.4} \cdot e^{-\frac{z/L_{a-V}}{0.12}} \quad (21)$$

$$\frac{L_{a-V}}{D} = (0.0022Re - 63.6) Ar^{0.053} \quad (22)$$

$$u_{p-ss-V} = v - u_t \quad (23)$$

where BR_{H-V} is the particle velocity ratio at bend point, u_{Bo-V} is the bend point outlet particle velocity (m/s), u_{Bi-V} is the bend point inlet particle velocity (m/s), Ar is the Archimedes number, R is the bend radius (m), D is the tube diameter (m), Re_{p-ss-V} is the particle Reynolds number at steady-state velocity in the vertical pipe, ρ_p is the particle density (kg/m^3), v is the air velocity (m/s), u_t is the particle terminal velocity (m/s), d is the particle diameter (m), μ is the air dynamic viscosity (Pa·s), g is the acceleration due to gravity (m/s^2), ρ_f is the air density (kg/m^3), L_{a-H} is the horizontal particle acceleration length (m), D_{50} is a reference diameter (50×10^{-3} m), Re_g is the gas Reynolds number, u_{p-ss-H} is the horizontal steady-state particle velocity (m/s), u_{p-H} is the particle velocity as a function of tube location in an horizontal tube (m/s), x is the horizontal distance from the seed feeding point (m), u_{p-V} is the particle velocity as a function of tube location in a vertical tube (m/s), u_{p-ss-V} is the vertical steady-state particle velocity (m/s), z is the vertical distance from horizontal tube centerline (m), and L_{a-V} is the vertical particle acceleration length (m).

Seed attributes (trajectory, velocity, drag force, and contact force) were recorded during each simulation. The seed contact force was defined as the sum of seed-seed and seed-wall forces acting on each seed. Regression analysis and paired t -test were used to determine trends and differences in seed attributes. Dimensional analysis was specifically applied to the data from simulation set 3 to study elbow geometry effects on seed contact force. All data post-processing and statistical analysis performed in this study were evaluated with RStudio (RStudio, Inc., Boston, MA, USA). RStudio libraries used during various data analysis steps are shown in Table 4.

Table 4. RStudio libraries used for data analysis.

Library Name	Function	Reference
readxl	Data processing	[33]
tidyverse	Data processing, plot generation	[34]
ggfortify	Plot generation	[35]
ggpointdensity	Plot generation	[36]
car	Statistical analysis	[37]
broom	Statistical analysis	[38]
lsmeans	Statistical analysis	[39]

3. Results and Discussion

3.1. Seed Trajectory

3.1.1. Effect of Air Velocity on the Seed Trajectory

Seed trajectory data for one-way coupled simulations at a seed rate of 0.07 kg/s and air velocities of 20, 25, and 30 m/s (Set 1) were considered in this section. Seeds generally traveled through the lower half of the tube until arrival at the elbow inlet, where two types of seed trajectories were observed (Figure 4a). The first trajectory type consisted of seeds that continued to slide across the elbow outer wall due to the centrifugal effect within the bend area. Sliding seeds maintained their trajectory for approximately 1 m in the

z-direction before gradually dispersing across the tube cross-section. The second trajectory type consisted of seeds that experienced a sudden direction change due to seed–seed and seed–wall impacts within the elbow area. A large portion of impacting seeds with trajectories directed away from the outer tube wall was redirected towards the primary airflow near the bend outlet (Figure 4b) and merged with the flow of sliding seeds. The principal airflow characteristics were qualitatively compared to a similar work [10] and were found to be in agreement. There were no observable particle trajectory patterns in the y -axis (perpendicular to the x - z plane). This was likely because particle Reynolds numbers, ranging between 10,000 and 16,000, were within Newton’s regime and were not significantly affected by secondary flow patterns. Results for one-way coupled simulations at the baseline seed rate of 0.07 kg/s generally followed similar patterns between the different air velocities (Figure 5). An analysis of variance (ANOVA) for the simulated data indicates no significant difference ($\alpha = 0.05$) between seed trajectories at different air velocities. However, a visual inspection of the average seed trajectories shown in Figure 5 suggests slight differences in the section closest to the bend area. Although the differences in average seed trajectory were not significant, the data do provide an indication of a slight increase in the number of impacting seeds with increased air velocity. A study performed by Yatskul et al. [1] recorded wheat seed trajectories on a smooth elbow using a high-speed camera. The wheat seeds in the smooth elbow experiments displayed both sliding and impacting trajectories similar to what is described by the pea simulation results. The proportion of impacting seeds was qualitatively described as larger in wheat for the experimental study than in our simulation results for peas. However, this is expected as the seed flow conditions for wheat also indicated a large number of suspended seeds in the horizontal section before the bend. Overall, simulated seed trajectories correlate well with experimental observations for similarly sized agricultural seeds.

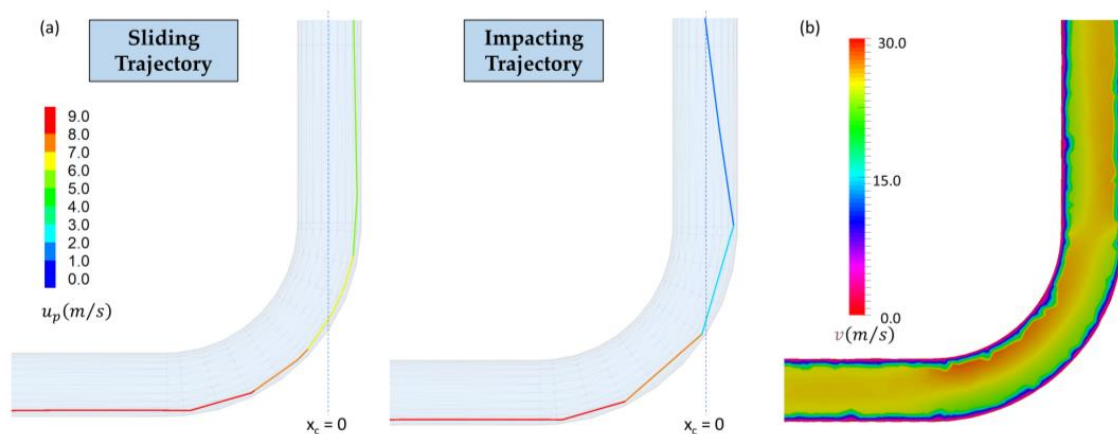


Figure 4. Simulated seed trajectory at a horizontal-vertical 90-degree elbow for 0.070 kg/s seed rate and air velocity (v) of 25 m/s: (a) seed path (u_p = Particle velocity, x_c = horizontal seed position relative to tube centerline), (b) sample airflow velocity profile.

3.1.2. Effects of Seed Rate on the Seed Trajectory

Seed trajectory data for one-way coupled simulations at an air velocity of 25 m/s and seed rates of 0.07, 0.21, and 0.42 kg/s (Set 2) were considered in this section. Visual examination of the data (Figure 6) suggests that only the 0.42 kg/s seed rate resulted in behavior that was noticeably different relative to the others. This was confirmed through statistical analysis. Seed trajectory data were not significantly different ($\alpha = 0.05$) between seed rates of 0.07 kg/s and 0.21 kg/s, $t(39) = -0.41$, $p = 0.68$. However, seed trajectory data for the seed rate of 0.42 kg/s, under the same airflow conditions, was significantly different ($\alpha = 0.05$) relative to the baseline seed rate of 0.07 kg/s, $t(39) = -2.77$, $p = 9 \times 10^{-3}$. The 0.42 kg/s seed rate showed a more pronounced roping effect relative to the other two seed

rates. Particle roping behavior is commonly described as particles flowing as a continuous band along the elbow outer wall followed by a disintegration of the rope further down the tubing. The formation and disintegration of the particle rope were similar to the results of CFD-DEM simulations reported by Kuang et al. [13], which included a similar solid loading ratio and a particle size of 3.76 mm. Figure 7 provides a visual representation of seed trajectories at different seed rates close to the bend area. The disintegration of the particle rope occurred at a similar location regardless of the seed rate. This was likely due to the use of one-way coupling where the airflow effects on seeds remain constant. Additional two-way coupled simulations and experiments would be required to study the solid loading ratio limit at which one-way coupled simulations can still be relatively accurate in approximating particle rope behavior.

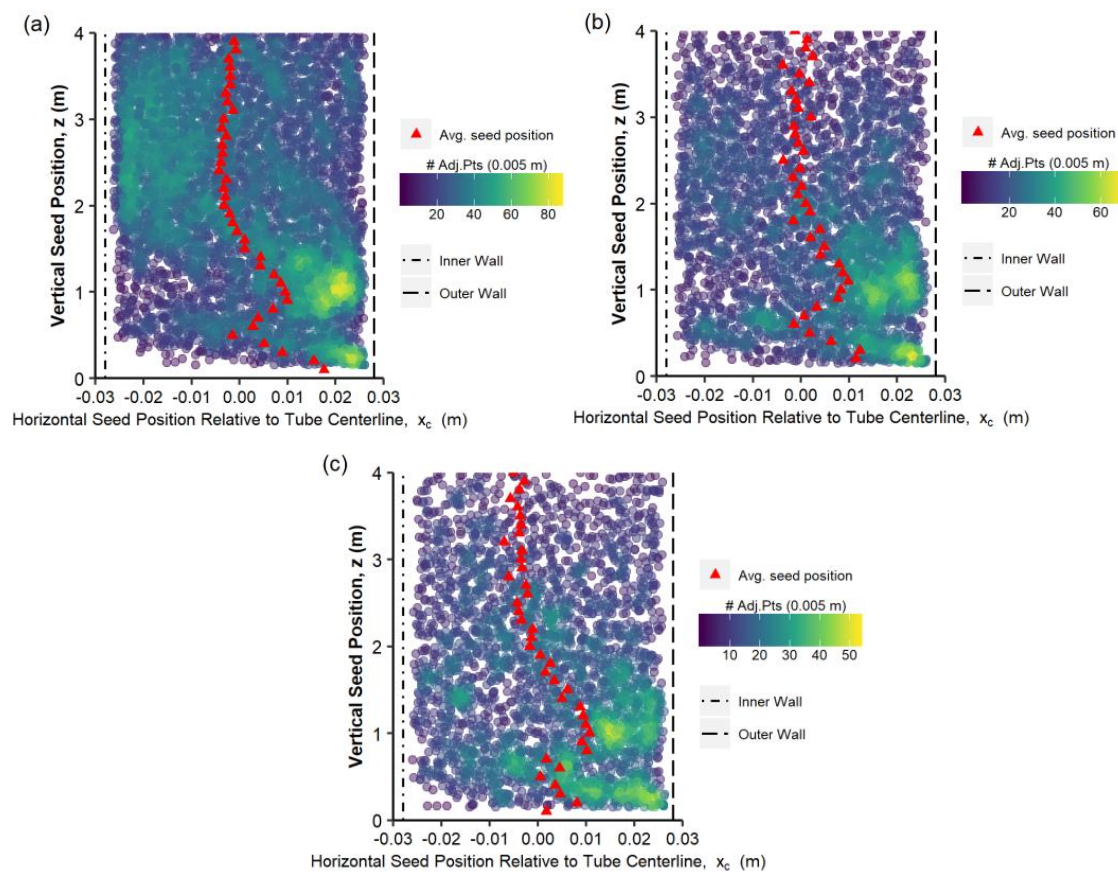


Figure 5. One-way coupled seed trajectory density plot, number (#) of adjacent points, and average seed positions for a seed rate of 0.070 kg/s and air velocities of (a) 20 m/s, (b) 25 m/s and (c) 30 m/s.

3.2. Seed Velocity

3.2.1. Effect of Air Velocity on the Seed Velocity

One-way coupled simulations at the baseline seed rate of 0.07 kg/s are discussed in this section (Set 1). Simulated average seed velocities generally described the calculated values (Equation (21)) with an overall coefficient of correlation (R^2) and mean square error (MSE) values of 0.85 and 0.67, respectively. The CFD-DEM simulation performed well considering calculated and experimental values reported by Thirpathi et al. [5] had differences within 10 to 20%. The velocity plots shown in Figure 8 provide a visualization of all recorded seed velocities. The data included within the red area shown in Figure 8 represent the bend transition, while the clear background represents the vertical tube section. Simulated seed velocities had a wider range of values closer to the elbow bend area. The seed velocity values merged approximately 1 m after the bend, which coincided with the seed trajectory data described in the previous section. Sliding seeds exiting the elbow had their

velocity reduced by approximately 50% while impacting seeds had their velocity reduced by approximately 80%. This was similar to the 60% average velocity reduction reported for experiments with wheat [1]. Simulated velocity plots (Figure 8) also indicated an increased number of impact trajectories with increased air velocity. This correlates well with previous observations noted in the seed trajectory section. Simulated velocities of impacting seeds had the best correlation to calculated values (Equation (21)). The study that derived these equations [5] originated from experimental measurements on smaller particles (less than 4 mm) that are more likely to exhibit suspended particle flow. This could provide a possible explanation for the observed differences. However, experiments replicating the simulated flow conditions (i.e., the stratified flow of larger particles) would be required to confirm this possibility. Acceleration lengths for the vertical tube section were calculated as 17, 24, and 30 m (Equation (22)) for air velocities of 20, 25, and 30 m/s, respectively. Steady-state seed velocities for the vertical tube section were calculated as 3, 8, and 13 m/s (Equation (23)) for air velocities of 20, 25, and 30 m/s, respectively. Whether a seed would accelerate or decelerate after exiting the elbow was affected by seed trajectory and collisions. Simulated air velocities of 25 and 30 m/s resulted in seeds generally accelerating within the vertical tube section. The simulations with 20 m/s air velocity resulted in many seeds decelerating. The simulation domain size was not large enough to determine a simulated steady-state seed velocity. However, seeds approached their respective vertical steady-state velocities as they travelled through the simulated tube length.

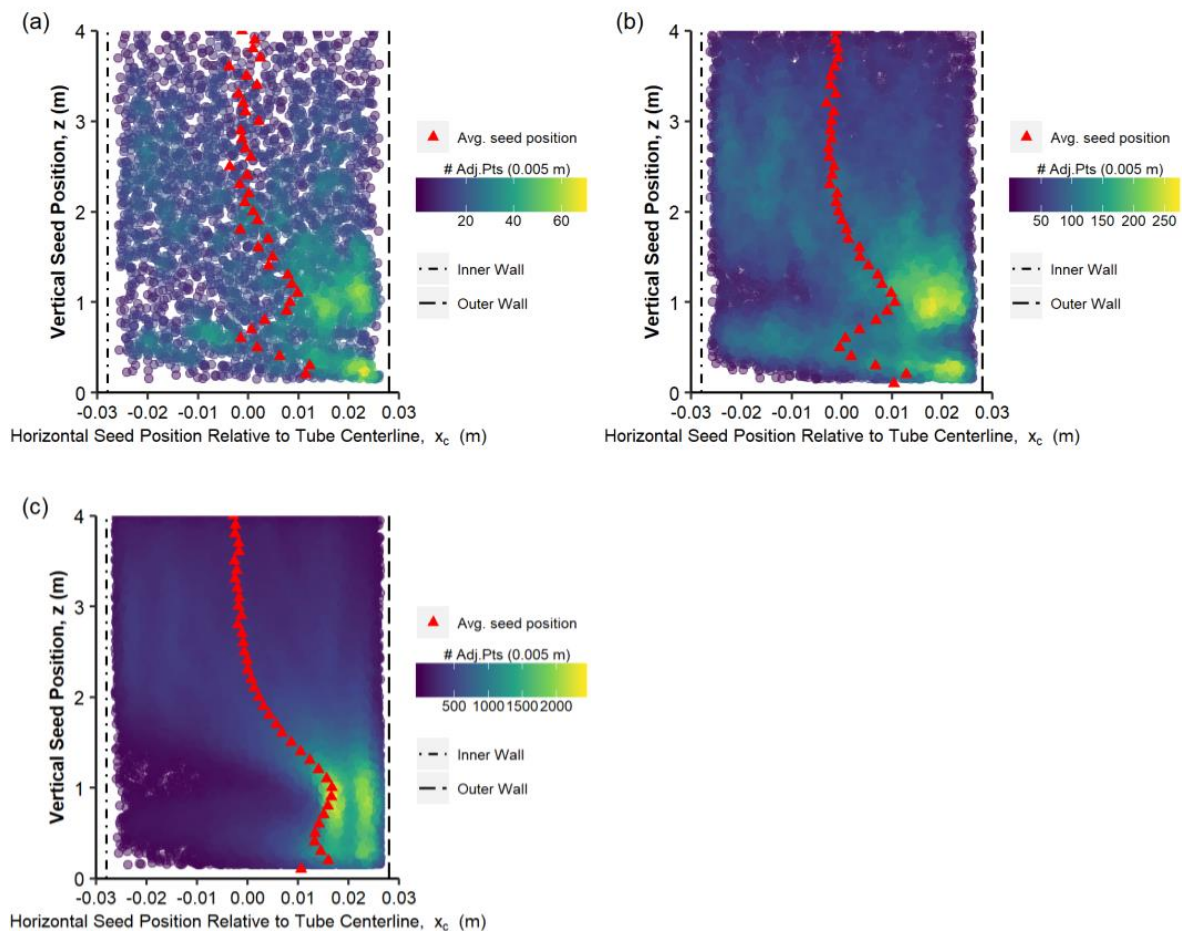


Figure 6. Seed trajectory density plot, number (#) of adjacent points, and average seed positions for 25 m/s air velocity and seed rates of (a) 0.07 kg/s, (b) 0.21 Kg/s and (c) 0.42 kg/s.

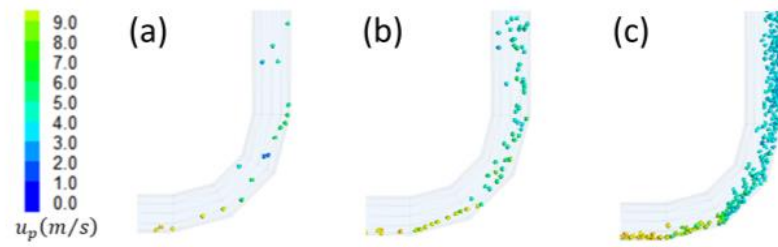


Figure 7. One-way coupled seed trajectory in horizontal-vertical 90-degree elbow for air velocity of 25 m/s and seed rates of (a) 0.07 kg/s, (b) 0.21 kg/s and (c) 0.42 kg/s.

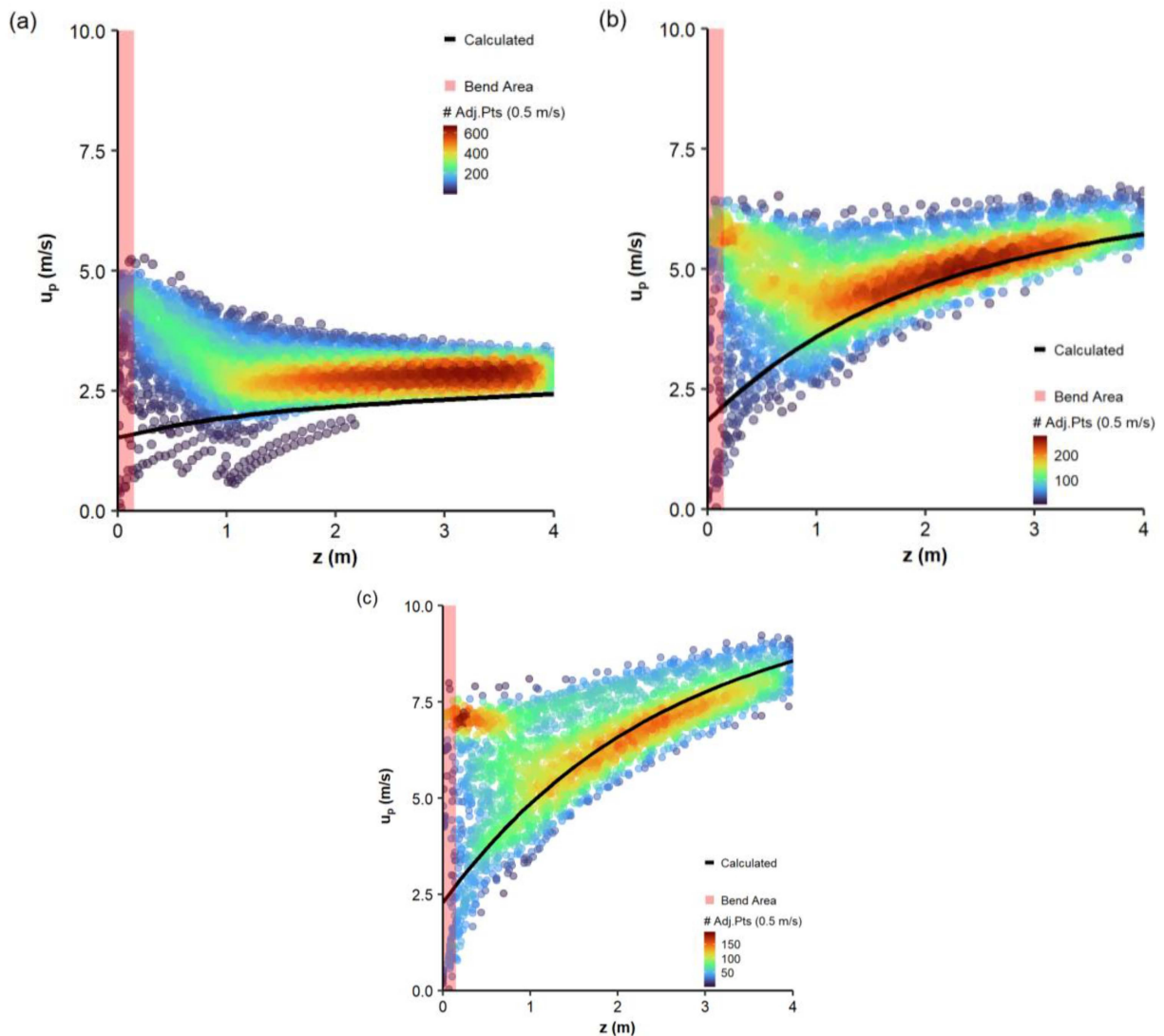


Figure 8. One-way coupled simulation density plot, number (#) of adjacent points, data for seed velocities (u_p) along the vertical tube section (z) at seed rate of 0.07 kg/s and air velocities of (a) 20 m/s, (b) 25 m/s, and (c) 30 m/s.

3.2.2. Effects of Seed Rate on the Seed Velocity

Seed velocity data for one-way coupled simulations at an air velocity of 25 m/s and seed rates of 0.07, 0.21, and 0.42 kg/s (Set 2) were considered in this section. The effect of seed rate was found to be significant ($\alpha = 0.05$) through an ANOVA. A representation of the data is shown in Figure 9. The difference in behavior was most noticeable by comparing seed velocity data points from the smallest and largest seed rate (Figure 9a,c). The effect

of seed collisions at higher seed rates influenced seed velocity profiles by reducing their average value. The effect of seed rate as described by the simulations was somewhat limited to the area near the bend because these were one-way coupled simulations. However, decreasing the seed velocities at the elbow exit caused the overall velocity profile to shift. Calculated seed velocities shown in Figure 9 provide a baseline for comparison purposes. Linear regression results from comparing average simulated seed velocity to calculated seed velocity values are shown in Table 5. The simulation at 0.07 kg/s seed rate had the best correlation to calculated values. Other simulated seed rates, 0.21 kg/s and 0.42 kg/s, had a relatively strong correlation to the calculated values but provide an indication that an additional solid loading ratio term might be needed to supplement the model proposed by Tripathi et al. [5]. Additional simulations and experiments working in parallel are still required to further document the effect of seed rate. Figure 9b,c reveal a few data points at the higher velocity range that were distinct from the main group of data points. Those data points represent the first few seeds entering the tube and were minimally affected by seed–seed collisions.

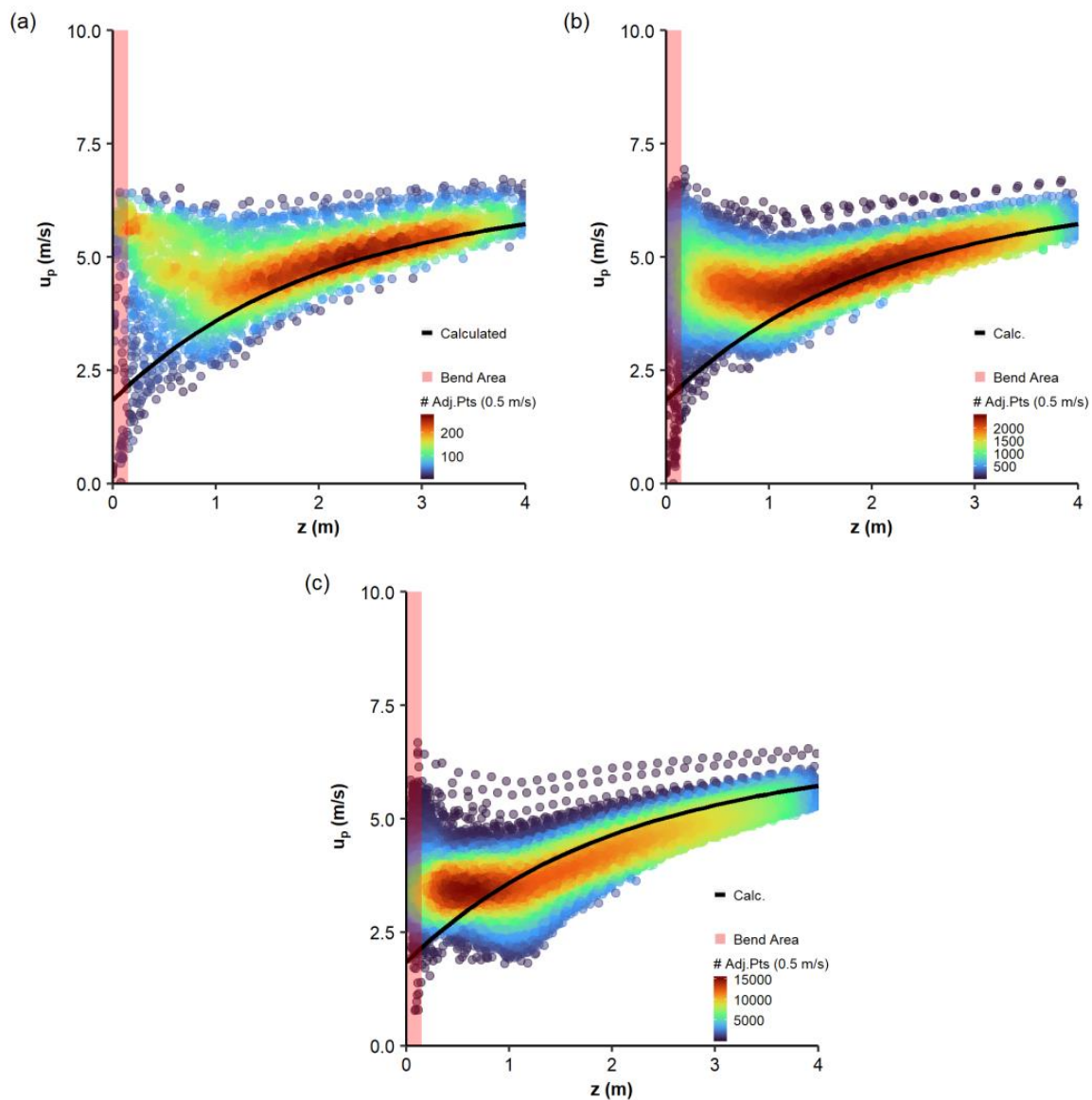


Figure 9. One-way coupled simulation density plot, number (#) of adjacent points, data for seed velocities (u_p) in horizontal-vertical 90-degree elbow along the vertical tube section (z) at air velocity of 25 m/s and seed rate of (a) 0.07 kg/s, (b) 0.21 kg/s, and (c) 0.42 kg/s.

Table 5. Coefficient of correlation (R^2) and mean square error (MSE) results for linear regression between simulated and calculated seed velocities at air velocity (V_a) of 25 m/s and multiple seed rates.

V_a (m/s)	Seed Rate (kg/s)	Linear Regression	
		R^2	MSE
25	0.07	0.93	0.16
	0.21	0.72	0.68
	0.42	0.81	0.46

3.3. Seed Force

3.3.1. Drag Force

Seed drag force data for one-way coupled simulations at the baseline seed rate of 0.07 kg/s and air velocities of 20, 25, and 30 m/s were considered in this section (Set 1). The drag force data followed patterns that were different for each elbow section. An example of location-specific drag forces for air velocity 25 m/s and one-way coupling is shown in Figure 10. Seeds in the horizontal section experienced almost constant drag force. As seeds passed through the elbow area the drag force increased at approximately half-way through the bend (45 deg). There was a lot more variation in the recorded drag force within the elbow area relative to the horizontal section. This was due to the combined effect of different types of seed trajectories, sliding and impact, as well as the nature of the airflow within the bend area. Seeds in the vertical tube section showed a wide range of drag forces within the first 1 m of the tube. This coincided with seed trajectories described in the previous section where seeds were redirected toward the outer wall by the airflow pattern. As the seeds travel further through the vertical tube, the average drag force was higher and had more variation relative to what was recorded in the horizontal tube section. This was due to seeds being able to freely traverse the vertical pipe cross-section rather than remain close to the tube wall. These patterns were consistent between different air velocities. Table 6 provides a summary of the average drag forces recorded for one-way coupled simulations.

Table 6. One-way coupled average drag force acting on seeds at various elbow sections at a seed rate of 0.07 kg/s.

V_a (m/s)	Average Seed Drag Force (N)		
	Horizontal Section	Bend Area	Vertical Section
20	0.0022	0.0029	0.0035
25	0.0027	0.0045	0.0048
30	0.0045	0.0067	0.0067

3.3.2. Contact Force

Seed contact force results from simulation set 3 are discussed in this section. Seed contact force within the elbow area was grouped by elbow diameter for visualization purposes. Figure 11 shows box plots of all seed contact forces recorded within the elbow area. The median was used to describe seed contact force for a given elbow diameter and bend radius combination as it is less susceptible to the large variations observed. The large variation in seed contact force values was due to the random nature of the seed collisions. The seed contact force data had a larger spread for a smaller elbow bend radius for any given elbow diameter. This was likely the effect of the impact angle on the seed trajectory with a larger bend radius having more sliding seeds relative to the smaller bend radius. The median contact force increased with elbow diameter for the 1.5D bend radius. However, the opposite trend was observed for the other elbow radii (2.5D, 3.5D, and 4.5D) where the median contact force decreased with elbow diameter for a given bend radius.

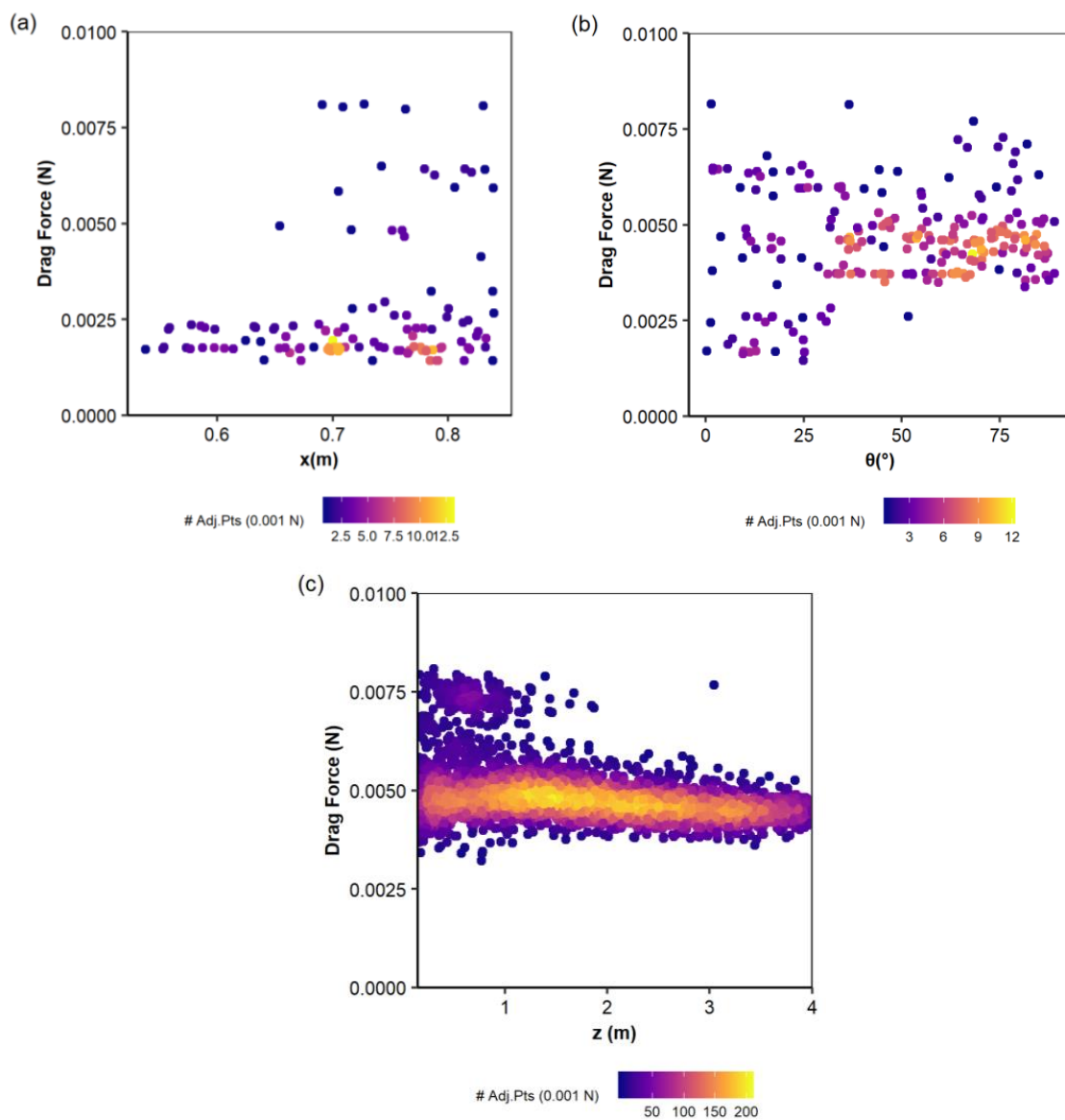


Figure 10. One-way coupled simulation density plot, number (#) of adjacent points, data showing seed drag force for air velocity of 25 m/s and seed rate of 0.07 kg/s at different elbow locations: (a) horizontal tube section (x), (b) angle within bend area (θ), and (c) vertical tube section (z).

3.3.3. Dimensional Analysis

The information obtained from simulation set 3 was used to generalize the effect of elbow geometry on seed contact force through dimensional analysis. Applying Buckingham's Pie theorem the following dimensionless groups were identified in the analysis:

$$\Pi_1 = \frac{F_{seed}}{\rho_f V_a^2 D^2} \quad (24)$$

$$\Pi_2 = \frac{\rho_f V_a D}{\mu} \quad (25)$$

$$\Pi_3 = \frac{R}{D} \quad (26)$$

$$\Pi_4 = \frac{d_p}{D} \quad (27)$$

$$\Pi_5 = \frac{\rho_p}{\rho_f} \quad (28)$$

$$\Pi_6 = \frac{\dot{m}_p}{\dot{m}_f} \quad (29)$$

where Π_1 is the dimensionless seed contact force, Π_2 is the gas Reynolds numbers, Π_3 is the ratio of the bend radius to the tube diameter, Π_4 is the ratio of the seed diameter to the tube diameter, Π_5 is the ratio of the seed density to the air density, and Π_6 is the ratio of the mass flow rate (\dot{m}_p) to the fluid flow rate (\dot{m}_f) or solids loading ratio (SLR).

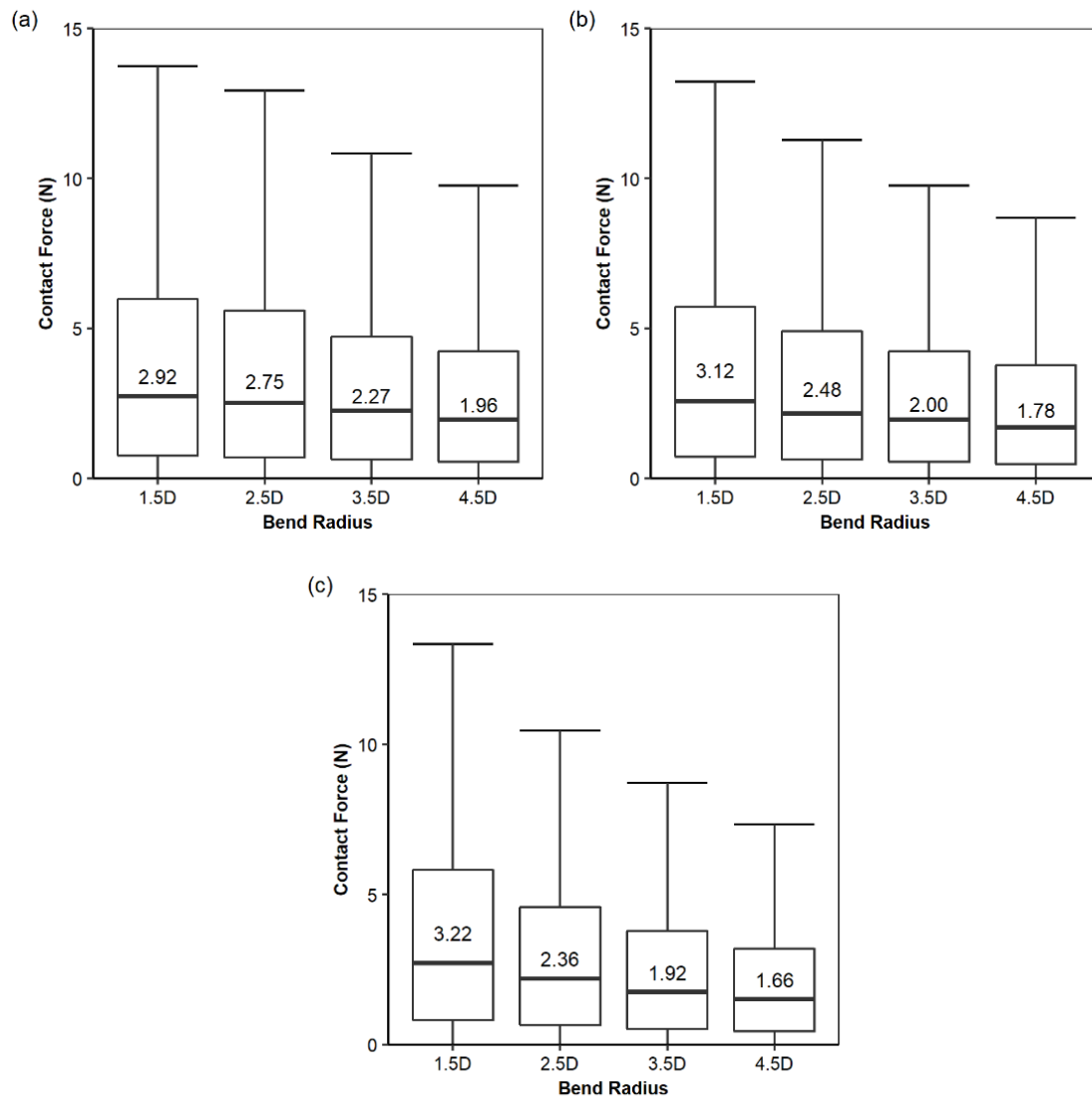


Figure 11. Seed contact force box plots at the elbow area as a function of bend radius for different elbow diameters: (a) 48.3 mm, (b) 60.3 mm, (c) 72.4 mm.

Then, the pie groups were arranged in the following form:

$$\frac{F_{seed}}{\rho_f V_a^2 D^2} = (Re)^a \left(\frac{R}{D}\right)^b \left(\frac{d_p}{D}\right)^c \left(\frac{\rho_p}{\rho_f}\right)^d \left(\frac{\dot{m}_p}{\dot{m}_f}\right)^e \quad (30)$$

where exponents a , b , c , d , and e are undetermined coefficients.

Considering that d_p , ρ_p , and SLR were constant in the simulation set 3, we can then simplify Equation (30) as:

$$\frac{F_{seed}}{\rho_f V_a^2 D^2} = K(Re)^a \left(\frac{R}{D}\right)^b \quad (31)$$

where the constant K and the exponents a , and b can be determined through multiple linear regression.

Obtaining the constant and coefficients from the multiple linear regression the relationship was:

$$\frac{F_{seed}}{\rho_f V_a^2 D^2} = 2.3 \times 10^{11} (Re)^{-2.2} \left(\frac{R}{D}\right)^{-0.5} \quad (32)$$

Figure 12 provides a visual representation of the regression analysis relative to the simulated data. The coefficient of correlation (R^2) was 0.9946 and the slope of 1.005 show the regression fit relative to the simulation data.

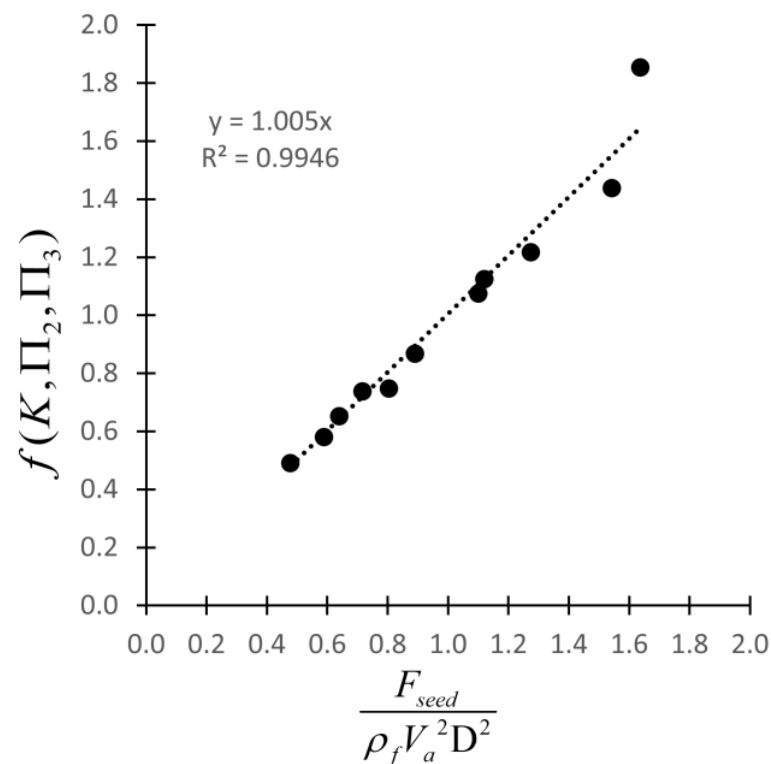


Figure 12. Relationship between Pi groups and dimensionless seed contact force.

Rearranging the terms in Equation (32) to examine elbow diameter and radius results in the following:

$$F_{seed} \propto D^{0.26} \quad (33)$$

$$F_{seed} \propto R^{-0.5} \quad (34)$$

The dimensional analysis results indicate the seed contact force, F_{seed} , is proportional to the elbow diameter, D , to the power of 0.26 and inversely proportional to the elbow bend radius, R , to the power of 0.5. This correlates well with the data presented in Figure 11. While both elbow diameter and radius influence seed contact force, dimensional analysis shows that selecting tube sizes that allow for a larger bend radius would be beneficial to reduce the magnitude of seed collision forces at the bend area.

3.4. Comparisons between One-Way and Two-Way Coupled Simulations

3.4.1. Seed Trajectory

Seed trajectory data for two-way coupled simulations followed patterns that were nearly identical to one-way coupled simulations for the conditions described in simulation set 1. Figure 13 provides a visual representation of two-way coupled seed trajectories which can be directly compared to Figure 5. For the purposes of seed trajectory approximation, the presence of particles did not affect airflow enough to change particle trajectory significantly at the simulated seed rate of 0.07 Kg/s. Statistical analysis considering all results from simulation set 1 indicates no significant difference ($\alpha = 0.05$) between seed trajectories for one-way and two-way coupled simulations, $t(119) = -0.33$, $p = 0.74$.

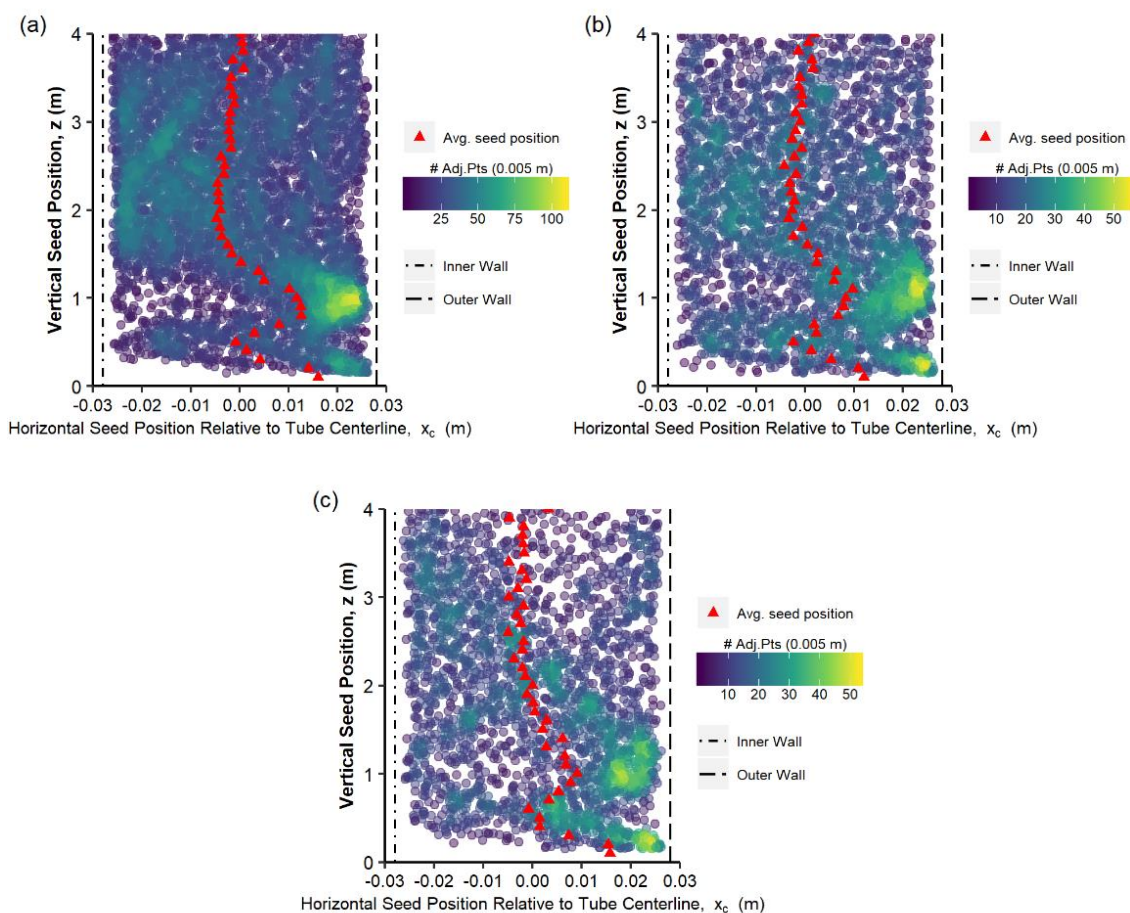


Figure 13. Two-way coupled seed trajectory density plot, number (#) of adjacent points, and average seed positions for a seed rate of 0.07 kg/s and air velocities of (a) 20 m/s, (b) 25 m/s, and (c) 30 m/s.

3.4.2. Seed Velocity

Seed velocity data for two-way and one-way coupled simulations are compared in this section (Set 1). Seed velocity average values were approximately 0.5 m/s higher for two-way coupled simulations and had a statistically significant difference ($\alpha = 0.05$) relative to one-way coupled simulations, $t(119) = -10.1$, $p < 2 \times 10^{-16}$. The source of the statistical differences was traced to seed velocities at the elbow area. This was due to constant updates of fluid fields (air velocity and pressure) to account for the presence of particles. Comparison between two-way coupled simulations and calculated values (Equation (21)) yielded R^2 and MSE values of 0.65 and 1.83, respectively. Figure 14 shows the seed velocity data for two-way coupling and can be directly compared to simulation conditions shown in Figure 8. Although numerical differences are present, one could argue that seed velocity trends were generally captured by both methods.

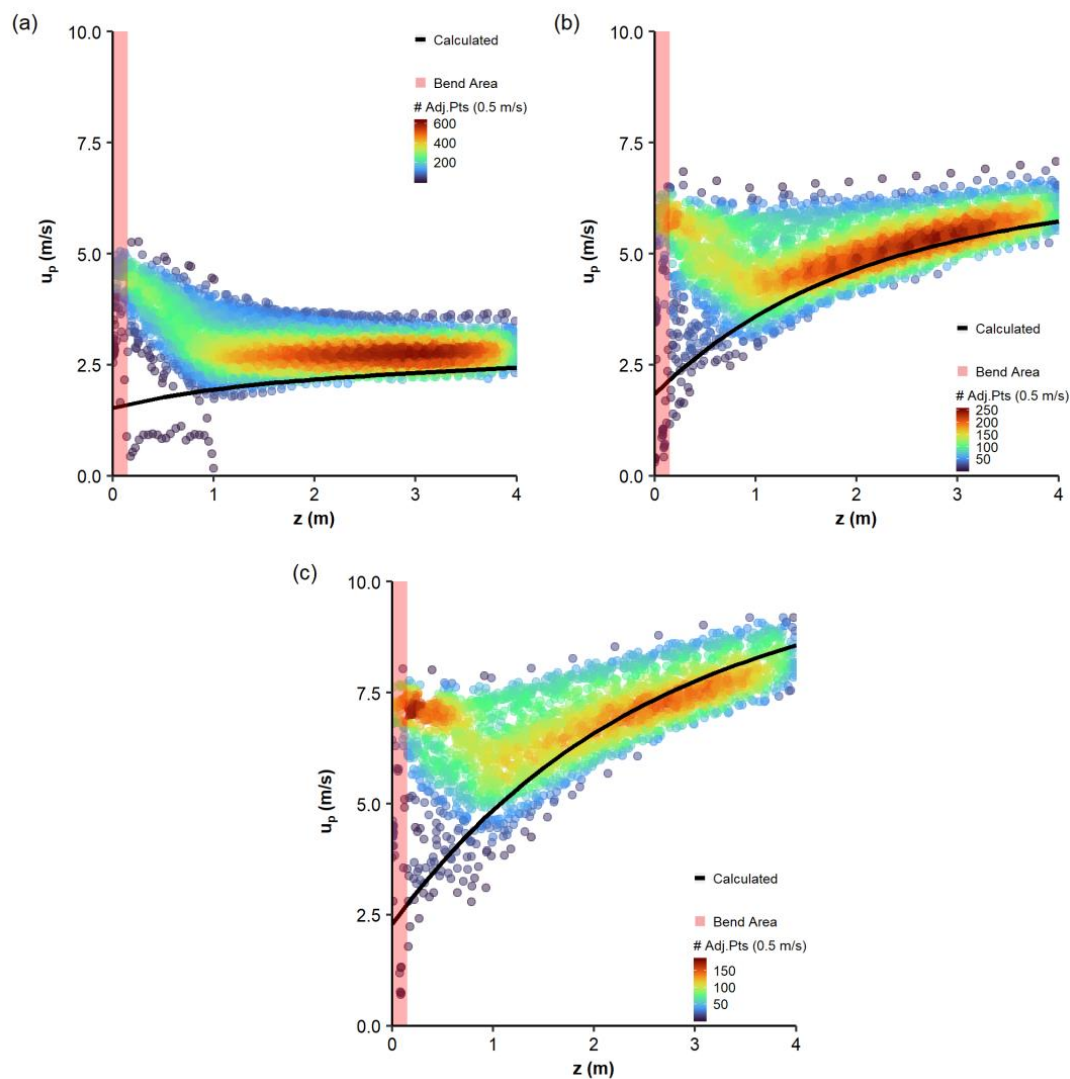


Figure 14. Two-way CFD-DEM coupled simulation density plot, number (#) of adjacent points, data for seed velocities (u_p) along the vertical tube section (z) at seed rate of 0.07 kg/s and air velocities of (a) 20 m/s, (b) 25 m/s, and (c) 30 m/s.

3.4.3. Seed Drag Force

Seed drag force data for two-way and one-way coupled simulations (Set 1) are compared in this section. Location-specific drag force values, Tables 6 and 7, were not significantly different ($\alpha = 0.05$) between coupling methods, $t(8) = -0.99$, $p = 0.35$. This indicates that the presence of particles was not sufficient to significantly affect the simulated drag force. However, seed velocity results showed some evidence of the influence of the airflow fields. Unfortunately, recording of pressure gradient acting on a particle at a given timestep is currently not supported in the PFC3D environment. Since drag force was found to be not significantly different, it is likely that the pressure gradient in combination with the air velocity influenced the seed velocity results. An example of location-specific drag forces for air velocity 25 m/s and two-way coupling is shown in Figure 15. The results shown in Figure 15 can be directly compared to Figure 10. Overall, the drag force patterns were similar regardless of the coupling method under the simulated conditions. Recorded drag force values were within the range reported by Lei et al. [40], who performed two-way coupled simulations under similar conditions.

Table 7. Two-way coupled average drag force acting on seeds at various elbow sections at a seed rate of 0.07 kg/s.

V_a (m/s)	Average Seed Drag Force (N)		
	Horizontal Section	Bend Area	Vertical Section
20	0.0015	0.0029	0.0035
25	0.0025	0.0045	0.0048
30	0.0055	0.0066	0.0063

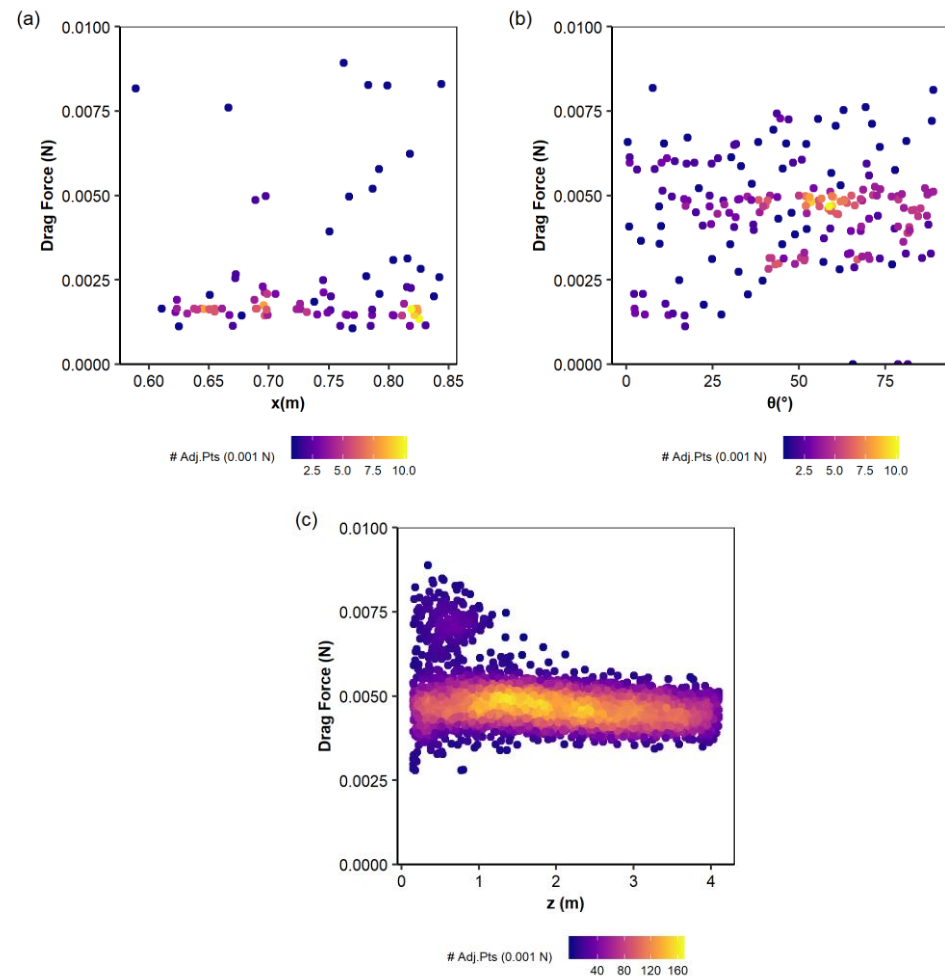


Figure 15. Two-way coupled simulation density plot, number (#) of adjacent points, data showing seed drag force for air velocity of 25 m/s and seed rate of 0.07 kg/s at different elbow locations: (a) horizontal tube section (x), (b) angle within bend area (θ), and (c) vertical tube section (z).

4. Conclusions

Seed attributes within a horizontal-vertical elbow transition were examined in detail through CFD-DEM coupled simulations. Two types of seed trajectory were generally observed: sliding across the elbow outer wall and sudden direction change after impacts in the elbow area. The ratio between sliding and impacting seed trajectories within the elbow transition was affected by air velocity and seed rate. Simulated seed velocities generally described the trends determined through current pneumatic conveyance theory. However, examining differences in seed trajectory showed a better correlation between impacting seeds and theoretical calculations. Comparison between one-way and two-way CFD-DEM coupling methods indicated that seed trajectory and drag force were not significantly affected for the simulated conditions, while seed velocity profiles were significantly different. Though it is important to recognize the numerical differences between simu-

lated seed velocity profiles in each coupling method, comparison to theoretical values showed that seed velocity trends were generally captured by both coupling methods at a seed rate of 0.07 kg/s. Overall results indicated that one-way coupling is a suitable option to describe seed flow in certain situations where two-way coupling may not be possible or practical. The effect of elbow diameter and bend radius on seed contact force was determined through dimensional analysis. This information can assist designers in trying to find the right balance between commercially available tube sizes and a bend radius that is manufacturable without costly tooling requirements. In the context of air seeders, considering elbow diameters that allow for larger bend radii may be desirable in future developments to reduce seed contact forces. Further experiments at higher seed rates would benefit theoretical calculations through the addition of a solids loading ratio term. Furthermore, future simulation work could introduce monitoring of seed distribution uniformity within air seeder systems (i.e., seed distributor head) where vertical sections are relatively short.

Supplementary Materials: The following supporting information can be downloaded at: <https://www.mdpi.com/article/10.3390/pr11030909/s1>, Figure S1: Steady-state air velocity (v) profile for 30 m/s inlet velocity at elbow mid-plane: (a) Moderate mesh, (b) Fine mesh; Table S1: Computational Fluid Dynamics (CFD) numerical schemes for OpenFOAM Sub-dictionaries; Table S2: Velocity measurements of 90-degree elbow steady-state airflow at bend inlet and bend outlet, rate of convergence (p), and Grid Convergence Index (GCI) for three mesh resolutions, with mesh length decreasing by factor of $r = 2$ between meshes.

Author Contributions: Conceptualization, L.G. and Y.C.; methodology, L.G. and Y.C.; software, L.G.; investigation, L.G.; writing—original draft preparation, L.G.; writing—review and editing, Y.C. and H.L.; visualization, L.G.; funding acquisition, Y.C. All authors have read and agreed to the published version of the manuscript.

Funding: This research was funded by the Natural Science and Engineering Research Council of Canada (RGPIN-2019-05861).

Data Availability Statement: The datasets used and/or analyzed during the current study are available from the corresponding author upon reasonable request.

Conflicts of Interest: The authors declare no conflict of interest.

References

1. Yatskul, A.; Lemiére, J.P.; Cointault, F. Influence of the Divider Head Functioning Conditions and Geometry on the Seed's Distribution Accuracy of the Air-Seeder. *Biosyst. Eng.* **2017**, *161*, 120–134. [[CrossRef](#)]
2. Baryeh, E.A. A Simple Grain Impact Damage Assessment Device for Developing Countries. *J. Food Eng.* **2003**, *56*, 37–42. [[CrossRef](#)]
3. Güner, M. Pneumatic Conveying Characteristics of Some Agricultural Seeds. *J. Food Eng.* **2007**, *80*, 904–913. [[CrossRef](#)]
4. Westerweel, J. Fundamentals of Digital Particle Image Velocimetry. *Meas. Sci. Technol.* **1997**, *8*, 1379–1392. [[CrossRef](#)]
5. Tripathi, N.M.; Santo, N.; Levy, A.; Kalman, H. Experimental Analysis of Velocity Reduction in Bends Related to Vertical Pipes in Dilute Phase Pneumatic Conveying. *Powder Technol.* **2019**, *345*, 190–202. [[CrossRef](#)]
6. Horabik, J.; Beczek, M.; Mazur, R.; Parafiniuk, P.; Ryzak, M.; Molenda, M. Determination of the Restitution Coefficient of Seeds and Coefficients of Visco-Elastic Hertz Contact Models for DEM Simulations. *Biosyst. Eng.* **2017**, *161*, 106–119. [[CrossRef](#)]
7. Manjula, E.V.P.J.; Ariyaratne, W.K.H.; Ratnayake, C.; Melaaen, M.C. A Review of CFD Modelling Studies on Pneumatic Conveying and Challenges in Modelling Offshore Drill Cuttings Transport. *Powder Technol.* **2017**, *305*, 782–793. [[CrossRef](#)]
8. Arastoopour, H. Numerical Simulation and Experimental Analysis of Gas/Solid Flow Systems: 1999 Fluor-Daniel Plenary Lecture. *Powder Technol.* **2001**, *119*, 59–67. [[CrossRef](#)]
9. Klinzing, G.E. A Review of Pneumatic Conveying Status, Advances and Projections. *Powder Technol.* **2018**, *333*, 78–90. [[CrossRef](#)]
10. Chu, K.W.; Yu, A.B. Numerical Simulation of the Gas-Solid Flow in Three-Dimensional Pneumatic Conveying Bends. *Ind. Eng. Chem. Res.* **2008**, *47*, 7058–7071. [[CrossRef](#)]
11. Laín, S.; Sommerfeld, M. Characterisation of Pneumatic Conveying Systems Using the Euler/Lagrange Approach. *Powder Technol.* **2013**, *235*, 764–782. [[CrossRef](#)]
12. Tsuji, Y.; Tanaka, T.; Ishida, T. Lagrangian Numerical Simulation of Plug Flow of Cohesionless Particles in a Horizontal Pipe. *Powder Technol.* **1992**, *71*, 239–250. [[CrossRef](#)]

13. Kuang, S.; Li, K.; Yu, A. CFD-DEM Simulation of Large-Scale Dilute-Phase Pneumatic Conveying System. *Ind. Eng. Chem. Res.* **2020**, *59*, 4150–4160. [[CrossRef](#)]
14. Furtney, J.; Zhang, F.; Han, Y. Review of Methods and Applications for Incorporating Fluid Flow in the Discrete Element Method. In Proceedings of the 3rd International FLAC/DEM Symposium, Hangzhou, China, 22–24 October 2013; pp. 1–10.
15. Liu, D.; Bu, C.; Chen, X. Development and Test of CFD-DEM Model for Complex Geometry: A Coupling Algorithm for Fluent and DEM. *Comput. Chem. Eng.* **2013**, *58*, 260–268. [[CrossRef](#)]
16. Marchelli, F.; Di Felice, R. A Comparison of Ansys Fluent and Mfix in Performing Cfd-Dem Simulations of a Spouted Bed. *Fluids* **2021**, *6*, 382. [[CrossRef](#)]
17. Xu, L.; Zhang, Q.; Zheng, J.; Zhao, Y. Numerical Prediction of Erosion in Elbow Based on CFD-DEM Simulation. *Powder Technol.* **2016**, *302*, 236–246. [[CrossRef](#)]
18. Vieira, R.E.; Mansouri, A.; McLaury, B.S.; Shirazi, S.A. Experimental and Computational Study of Erosion in Elbows due to Sand Particles in Air Flow. *Powder Technol.* **2016**, *288*, 339–353. [[CrossRef](#)]
19. Hong, B.; Li, X.; Li, Y.; Li, Y.; Yu, Y.; Wang, Y.; Gong, J.; Ai, D. Numerical Simulation of Elbow Erosion in Shale Gas Fields under Gas-solid Two-phase Flow. *Energies* **2021**, *14*, 3804. [[CrossRef](#)]
20. Balevičius, R.; Sielamowicz, I.; Mróz, Z.; Kačianauskas, R. Investigation of Wall Stress and Outflow Rate in a Flat-Bottomed Bin: A Comparison of the DEM Model Results with the Experimental Measurements. *Powder Technol.* **2011**, *214*, 322–336. [[CrossRef](#)]
21. Wiacek, J.; Molenda, M.; Horabik, J.; Ooi, J.Y. Influence of Grain Shape and Intergranular Friction on Material Behavior in Uniaxial Compression: Experimental and DEM Modeling. *Powder Technol.* **2012**, *217*, 435–442. [[CrossRef](#)]
22. Itasca. *PFC3D Particle Flow Code in 3 Dimensions, Verification Problems and Example Applications*; Itasca Consulting Group, Inc.: Minneapolis, MN, USA, 2017.
23. Guzman, L.J.; Chen, Y.; Landry, H. Discrete Element Modeling of Seed Metering as Affected by Roller Speed and Damping Coefficient. *Trans. ASABE* **2020**, *63*, 189–198. [[CrossRef](#)]
24. Roache, P.J. Perspective: A Method for Uniform Reporting of Grid Refinement Studies. *J. Fluids Eng. Trans. ASME* **1994**, *116*, 405–413. [[CrossRef](#)]
25. Roache, P.J. Quantification of Uncertainty in Computational Fluid Dynamics. *Annu. Rev. Fluid Mech.* **1997**, *29*, 123–160. [[CrossRef](#)]
26. Kalitzin, G.; Medic, G.; Iaccarino, G.; Durbin, P. Near-Wall Behavior of RANS Turbulence Models and Implications for Wall Functions. *J. Comput. Phys.* **2005**, *204*, 265–291. [[CrossRef](#)]
27. Versteeg, H.K.; Malalasekera, W. *An Introduction to Computational Fluid Dynamics: The Finite Volume Method*; Pearson Education: Harlow, UK, 2007.
28. OpenFOAM SimpleFoam. Available online: <https://github.com/OpenFOAM/OpenFOAM-3.0.x/tree/master/applications/solvers/incompressible/simpleFoam> (accessed on 20 January 2023).
29. Furtney, J. PFC3D_OpenFOAM. Available online: https://github.com/jkfurtney/PFC3D_OpenFOAM (accessed on 1 August 2017).
30. Guzman, L.; Chen, Y.; Landry, H. Coupled Cfd-Dem Simulation of Seed Flow in an Air Seeder Distributor Tube. *Processes* **2020**, *8*, 1597. [[CrossRef](#)]
31. Santo, N.; Portnikov, D.; Eshel, I.; Taranto, R.; Kalman, H. Experimental Study on Particle Steady State Velocity Distribution in Horizontal Dilute Phase Pneumatic Conveying. *Chem. Eng. Sci.* **2018**, *187*, 354–366. [[CrossRef](#)]
32. Santo, N.; Portnikov, D.; Tripathi, N.M.; Kalman, H. Experimental Study on the Particle Velocity Development Profile and Acceleration Length in Horizontal Dilute Phase Pneumatic Conveying Systems. *Powder Technol.* **2018**, *339*, 368–376. [[CrossRef](#)]
33. Wickham, H.; Bryan, J. Readxl: Read Excel Files R Package Version 1.3.1. 2019. Available online: <https://CRAN.R-project.org/package=readxl> (accessed on 20 January 2023).
34. Wickham, H. *Tidyverse: Easily Install and Load the “Tidyverse”*; R Core Team: Vienna, Austria, 2017.
35. Tang, Y.; Horikoshi, M.; Li, W. Ggfortify: Unified Interface to Visualize Statistical Result of Popular R Packages. *R J.* **2016**, *8*, 478–489. [[CrossRef](#)]
36. Kremer, L.P.M. *Ggpointdensity: A Cross between a 2D Density Plot and a Scatter Plot*; R Core Team: Vienna, Austria, 2019.
37. Fox, J.; Weisberg, S. *An {R} Companion to Applied Regression*; SAGE: Thousand Oaks, CA, USA, 2019.
38. Robinson, D.; Hayes, A. *Broom: Convert Statistical Analysis Objects into Tidy Tibbles*; R Core Team: Vienna, Austria, 2019.
39. Russel, V.L. Least-Squares Means: The R Package Lsmeans. *J. Stat. Softw.* **2016**, *69*, 1–33.
40. Lei, X.; Liao, Y.; Zhang, Q.; Wang, L.; Liao, Q. Numerical Simulation of Seed Motion Characteristics of Distribution Head for Rapeseed and Wheat. *Comput. Electron. Agric.* **2018**, *150*, 98–109. [[CrossRef](#)]

Disclaimer/Publisher’s Note: The statements, opinions and data contained in all publications are solely those of the individual author(s) and contributor(s) and not of MDPI and/or the editor(s). MDPI and/or the editor(s) disclaim responsibility for any injury to people or property resulting from any ideas, methods, instructions or products referred to in the content.